Thermal stability and deformation mechanisms in novel Ni-Co-Fe-Cr-Al-Ti-Nb-type nanoparticle-strengthened high-entropy alloys

Jinxiong Hou[a, b], Jianyang Zhang[a], Jixun Zhang[a], Junhua Luan[a], Boxuan Cao[c], Yilu Zhao[c]

Zengbao Jiao[d], X.J. Liu[c], P.K. Liaw[e], and Tao Yang[a, b,*]

[a] Department of Materials Science and Engineering, City University of Hong Kong, Hong Kong, China

[b] Hong Kong Institute for Advanced Study, City University of Hong Kong, Tat Chee Avenue, Kowloon Tong, Kowloon, China

[c] School of Materials Science and Engineering, Harbin Institute of Technology, Shenzhen, China

[d] Department of Mechanical Engineering, The Hong Kong Polytechnic University, Hong Kong, China

[e] Department of Materials Science and Engineering, The University of Tennessee, Knoxville, TN 37996-2200, USA

*Corresponding author at: taoyang6@cityu.edu.hk (Tao Yang)

Abstract

The precipitate morphology, coarsening kinetics, elemental-partitioning behaviors, grain structures, and tensile properties were explored in detail for $L1_2$-strengthened $Ni_{39.9}Co_{20}Fe_{15}Cr_{15}Al_6Ti_{4-x}Nb_xB_{0.1}$ (x = 0, 2, and 4) high-entropy alloys (HEAs). By substituting Ti with Nb, the spheroidal-to-cuboidal precipitate morphological transition, increase in the coarsening kinetics, and phase decomposition upon aging at 800 °C occurred. The excessive addition of Nb brings about the grain boundary-type Nb-rich phase along with phase decomposition from the $L1_2$ to lamellae-structured $D0_{19}$ phase upon the long-term aging duration. By partially substituting the Ti with Nb, the chemically complex and the thermally stable $L1_2$ phase with a composition of $(Ni_{58.8}Co_{9.8}Fe_{2.7})(Al_{12.7}Ti_{5.8}Nb_{7.5}Cr_{2.3})$ ensures the stable phase structure and clean grain boundaries, which guarantees the superb high-temperature tensile strength (791 ± 7 MPa for yielding and 1,013 ± 11 MPa for failure) at 700 °C. Stacking

faults (SFs) were proved to prevail during the plastic deformation, offering a high work-hardening capability at 700 °C. An anomalous rise in the yield strength at 800 ℃ was found, which could be ascribed to the multi-layered super-partial dislocations with a cross-slip configuration within the $L1_2$ particles.

Keywords: High-entropy alloys; Coarsening kinetics, Coherent precipitation strengthening; Mechanical properties

1. Introduction

As a new type of structural materials, coherent precipitation-strengthened high-entropy alloys (HEAs) are expected to possess unique mechanical properties [1]. Basically, the coherent A_3B-type crystal with an $L1_2$ structure can effectively reinforce the face-centered-cubic (FCC) matrix, enabling the high strengths of alloys at elevated temperatures [2]. However, most $L1_2$-type Ni_3Al phases in traditional superalloys are compositionally simple containing a relatively lower level of ternary elements, which generally leads to an obvious dilemma of strength-ductility tradeoff [3]. Recent studies showed that the multi-component alloying can help significantly improve the intrinsic strength and ductility of the $L1_2$ phase [4]. As a result, engineering compositionally complex $L1_2$ precipitates are expected to pave a promising avenue for designing novel HEAs towards superior thermal-mechanical performances [5-7].

It is worth mentioning that the addition of multiple elements and corresponding complex chemical interactions in these $L1_2$-strengthened HEAs usually produces undesired brittle phases along grain boundaries, such as the lamellae-like η and $L2_1$-type Heusler phases [8-10]. These detrimental intergranular phases will deteriorate their mechanical properties at both room and elevated temperatures, making them unsatisfactory for many practical high-temperature applications [9]. Similar behaviors have also been frequently observed in various conventional alloys. For instance, the Ni-Fe base superalloys that rely on the Ti addition for the metastable Ni_3Ti-type $L1_2$ strengthener undergo the $L1_2 \rightarrow \eta$ phase transformation upon long exposure at temperatures above 650 °C, leading to a great loss in strength [11]. The controllable alloying

of refractory elements (like Nb and Ta) is expected to effectively improve the tensile strengths of alloys [12-14]. On the one hand, the addition of them would generate a strong influence on the lattice parameters and associated interfacial coherency of the FCC/$L1_2$ structure, which thereby affects the strengthening efficiency [15]. On the other hand, however, an excessive addition of them will thermodynamically destabilize the FCC/$L1_2$ phase microstructure and leads to the formation of other brittle phases, such as the Laves and δ phases [16, 17]. This trend will in turn cause the increased crack susceptibility of alloys, as well as the deterioration of their strength and service life. Therefore, optimized alloying of refractory elements to improve the mechanical properties while maintaining a stable phase structure in the $L1_2$-strengthened HEAs is highly desired and of great scientific significance.

Along with this line of thinking, in the present study, we attempted to partially replace Ti with Nb in the $L1_2$-strengthened Ni-Co-Fe-Cr-Al-Ti-Nb-type HEA system. The variation of the Ti/Nb ratio on the coherent microstructure and associated mechanical properties was carefully evaluated. Based on this effort, we successfully obtained a high-strength and microstructurally stable HEA [$Ni_{39.9}Co_{20}Fe_{15}Cr_{15}Al_6Ti_2Nb_2B_{0.1}$, atomic percent (at.%)] strengthened by the multi-component (Ni, Co, Fe, Cr)$_3$(Al, Nb, Ti)-type $L1_2$ nanoparticles. The temporal evolutions of nanoparticles, mechanical properties, and corresponding deformation mechanisms of this novel HEA at both room and elevated temperatures were systematically investigated.

2. Experimental details

A series of alloys with the nominal compositions of $Ni_{39.9}Co_{20}Fe_{15}Cr_{15}Al_6Ti_4B_{0.1}$, $Ni_{39.9}Co_{20}Fe_{15}Cr_{15}Al_6Ti_2Nb_2B_{0.1}$, and $Ni_{39.9}Co_{20}Fe_{15}Cr_{15}Al_6Nb_4B_{0.1}$ (at.%) were developed to obtain the "FCC + $L1_2$" dual-phase microstructure. For convenience, the alloys were named as the Al_6Ti_4, $Al_6Ti_2Nb_2$, and Al_6Nb_4 HEAs hereafter according to the specific contents of Al, Ti, and Nb. The ingots were prepared by mixing the individual pure metal of Co, Cr, Fe, Ni, Ti, Nb, B, and Al [purity larger than 99.9 weight percent (wt.%)] in an arc-melting furnace under an Ar atmosphere and then casted into a copper mold with the dimension of 50 × 12 × 5 mm^3. Each ingot button was melted at least five times to ensure the homogenization of compositions. High-temperature homogenization treatment at 1,150 ℃ for 2 h was conducted to eliminate the

as-cast dendrite structures. The as-homogenized HEAs were cold rolled with a thickness reduction of 65% and then recrystallized at 1,150 ℃ for 2.5 min. Subsequently, the recrystallized sheets were aged at 800 ℃ for various durations from 24 h to 336 h to evaluate their microstructural stabilities.

The as-aged samples were mechanically and electrochemically polished, and then analyzed by scanning electron microscope (SEM, FEI Scios) equipped with an electron backscattered diffraction (EBSD) detector. The lattice constant was measured by a high-resolution X-ray diffraction (XRD, Bruker D2) test from 20° to 90° with a scan rate of 0.5°/min. The lattice misfit was determined by deconvolution (pseudo-Voigt function fit) of the (220) diffraction peak, following the equation of $\delta = 2(\alpha_{\text{particle}} - \alpha_{\text{matrix}})/(\alpha_{\text{particle}} + \alpha_{\text{matrix}})$, in which the α refers to the lattice parameter of each phase. The diameters of nanoparticles were collected by the commercial ImageJ software, which were estimated by using the equivalent circle radius method [18], and the average equivalent circle diameter was calculated according to the following formula: $a_P = 2\sqrt{A_p/\pi}$, and $\bar{a} = \frac{1}{n}\sum_{i=1}^{n} a_P^i$, where A_P is the area of the precipitation, a_P is the equivalent circle diameter of the precipitates, n is the total number of precipitates involved. The phase components and microstructures were further observed by the transmission electron microscope (TEM, JEOL 2100F), and the detailed chemical compositions of the phases were obtained by the energy dispersive X-ray spectroscopy (EDS) in scanning transmission electron microscopy (STEM), as well as the atom probe tomography (APT, LEAP 5000XR). The tensile tests for the aged (800 ℃, 24 h) samples with a gauge length of 12.5 mm and a width of 3.2 mm were used to measure the mechanical properties at room and high temperatures in an air condition.

3. Results

3.1 Microstructures and compositional partitioning behaviors

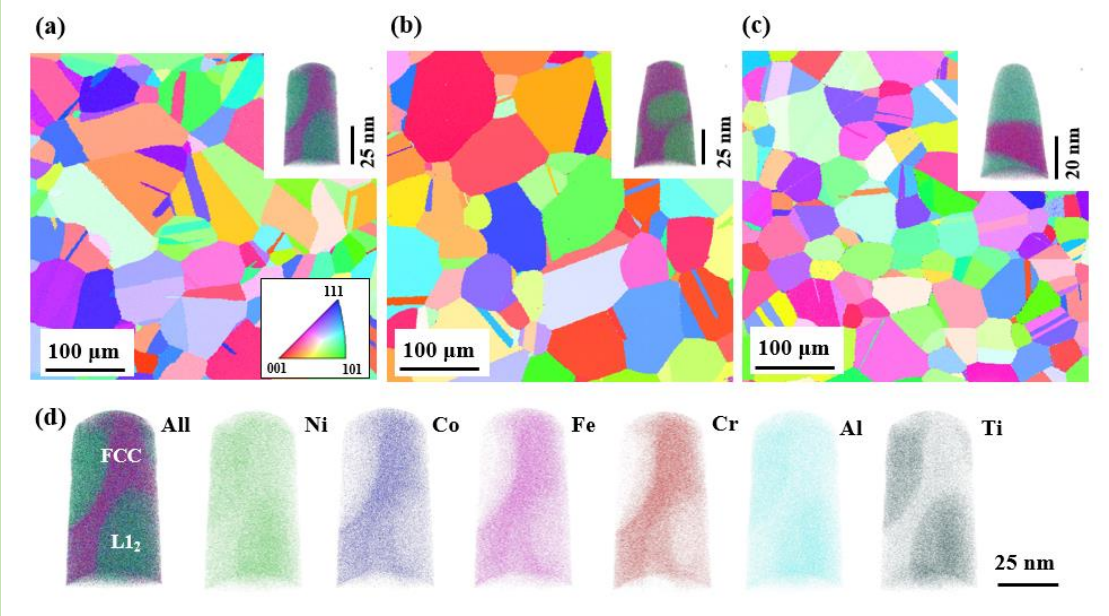

Fig. 1 The EBSD inverse pole figures (IPFs) of (a) Al_6Ti_4, (b) $Al_6Ti_2Nb_2$, and (c) Al_6Nb_4 HEAs showing the fully recrystallized microstructures. (d) Reconstruction of the elemental distributions in the interior grain of Al_6Ti_4 HEA after aging at 800 ℃ for 24 h, exhibiting the elemental partitioning behaviors between the FCC and $L1_2$ phases. The inserts in (a ~ c) show the all-element distributions in the interior grains by APT.

Figure 1 shows the EBSD IPFs of the Al_6Ti_4, $Al_6Ti_2Nb_2$, and Al_6Nb_4 HEAs. All the microstructures contain equiaxed grains with annealing twins within some of the grains. The average grain size of Al_6Ti_4 HEA is 55.1 ± 20.2 μm, which could be decreased by the substitution of Nb for Ti. As a result, the Al_6Nb_4 HEA has an average grain size of 46.8 ± 18.9 μm. The inserts in **Figs. 1a-c** present the all-element distributions between the FCC and $L1_2$ phases in the Al_6Ti_4, $Al_6Ti_2Nb_2$, and Al_6Nb_4 HEAs by the APT measurement, respectively. Specifically, the elemental distributions between the FCC and $L1_2$ phases in the Al_6T_4 HEA were separately displayed in **Fig. 1d**, from which the compositional partitioning behaviors with a strong tendency of Ni, Al, and Ti in $L1_2$ nanoparticles whilst Fe, Co, and Cr in the matrix of Al_6Ti_4 HEA can be clearly identified.

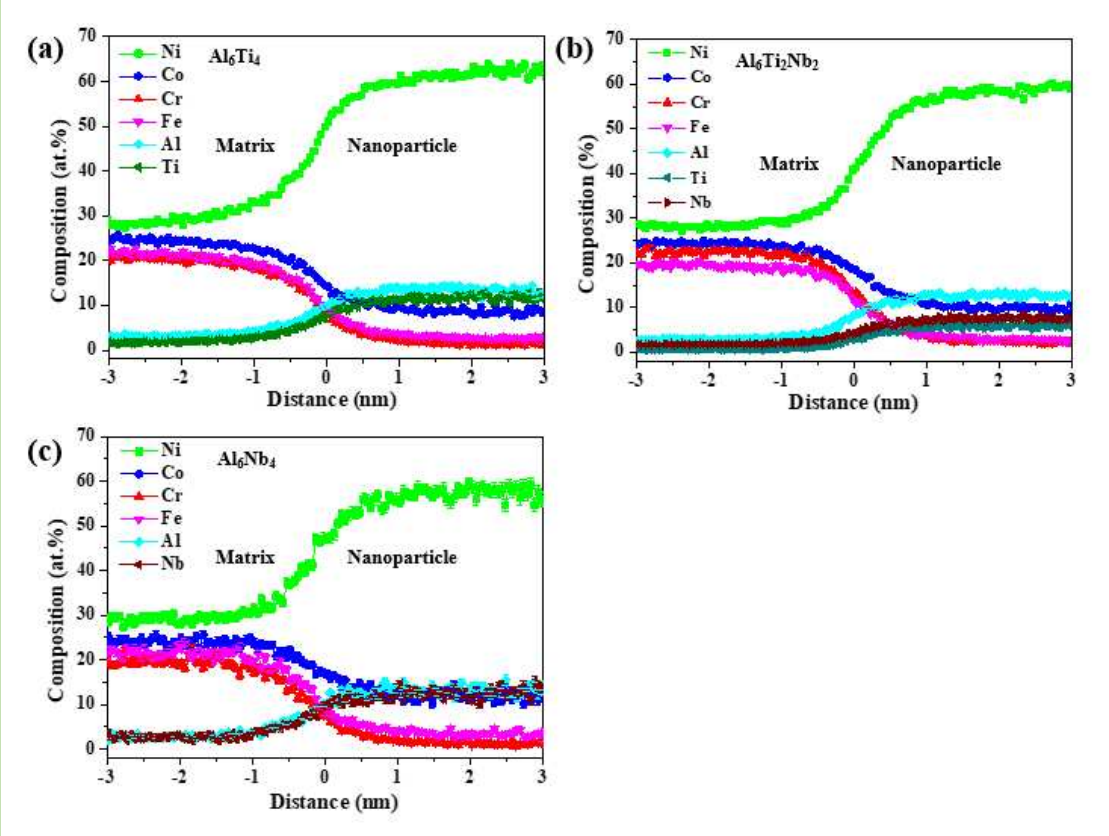

Fig. 2 The chemical composition variations between the FCC-type matrix and $L1_2$-type nanoparticles in the (a) Al_6Ti_4, (b) $Al_6Ti_2Nb_2$, and (c) Al_6Nb_4 HEAs.

Figure. 2 exhibits the chemical composition profiles between the FCC and $L1_2$ phases in the present alloy system. The detailed compositions were listed in **Table. 1**, the multi-component $(Ni_{62.1}Co_{8.9}Fe_{2.9})(Al_{14.1}Ti_{12.0}Cr_{2.5})$ is assumed as the stoichiometry of the $L1_2$ phase in the Al_6Ti_4 HEA. Due to Nb acting as a strong $L1_2$-forming element, after substituting the Ti with Nb partially, the multi-component $(Ni_{58.8}Co_{9.8}Fe_{2.7})(Al_{12.7}Ti_{5.8}Nb_{7.5}Cr_{2.3})$ is confirmed as the stoichiometry of the $L1_2$ phase in the $Al_6Ti_2Nb_2$ HEA from the APT analysis [19]. With the further substitution of Ti by Nb, the multi-component $(Ni_{59.2}Co_{9.8}Fe_{3.1})(Al_{12.9}Nb_{12.7}Cr_{1.6})$-type $L1_2$ phase is formed in the Al_6Nb_4 HEA.

Table. 1 Chemical compositions of the FCC-type matrix and $L1_2$-type nanoparticles in the Al_6Ti_4, $Al_6Ti_2Nb_2$, and Al_6Nb_4 HEAs.

Alloy	Phase	Compositions (at. %)						
		Ni	Co	Fe	Cr	Al	Ti	Nb
Al_6Ti_4	FCC	28.2	25.2	21.5	20.1	3.1	1.9	/
	$L1_2$	62.1	8.9	2.9	2.5	14.1	12.0	/
$Al_6Ti_2Nb_2$	FCC	28.1	24.5	22.1	19.8	3.0	0.8	1.7
	$L1_2$	58.8	9.8	2.7	2.3	12.7	5.8	7.5
Al_6Nb_4	FCC	29.6	23.8	21.3	19.9	2.5	/	2.8
	$L1_2$	59.2	9.8	3.1	1.6	12.9	/	12.7

3.2 Temporal evolutions of the intragranular $L1_2$-type nanoprecipitates

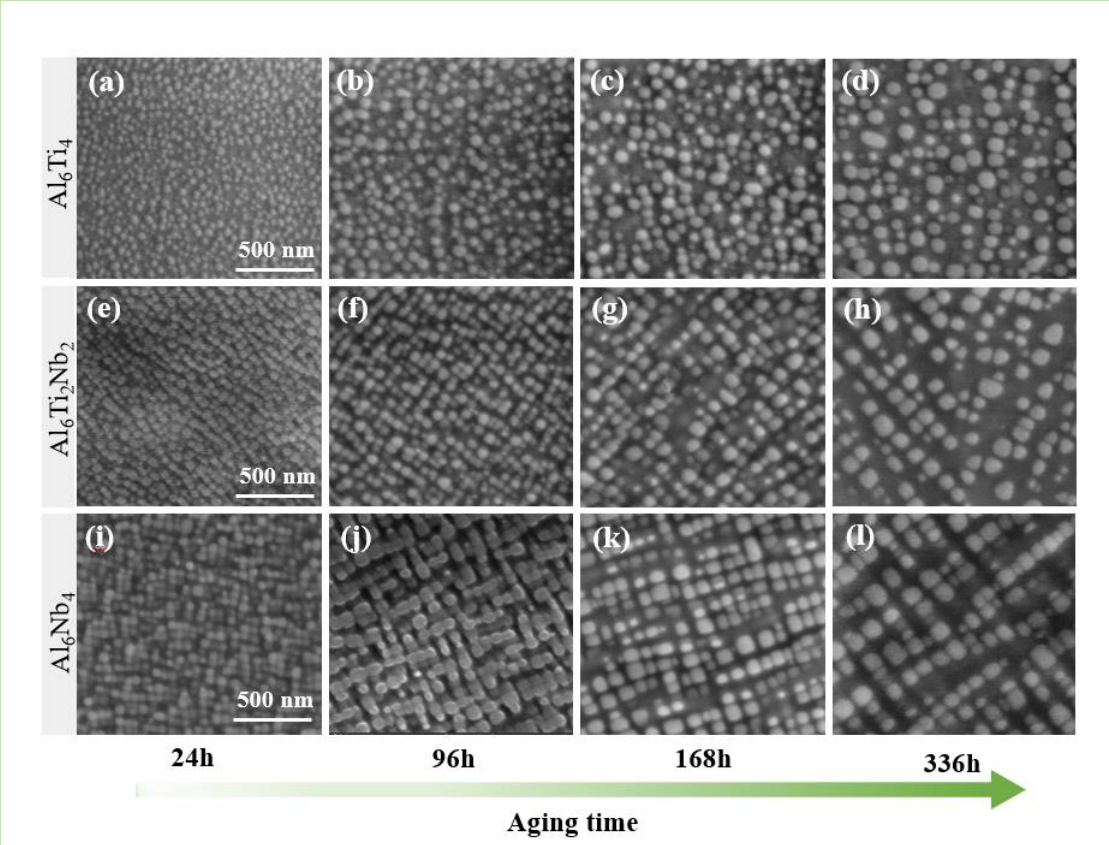

Fig. 3 Temporal evolutions of the intragranular $L1_2$-type nanoprecipitates in the (a ~ d) Al_6Ti_4, (e ~ h) $Al_6Ti_2Nb_2$, and (i ~ l) Al_6Nb_4 HEAs after aging at 800 °C for 24 h, 96 h, 168 h, and 336 h, respectively.

As shown in **Fig. 3**, aging at 800 ℃ induced the uniformly distributed nanoprecipitates in the interiors of grains in the present alloy system, where the size of nanoprecipitates presents a continuous increase with the aging time that occurs concomitantly with a decrease in the number density of precipitate. The average size of precipitated particles (in diameter) was quantitatively analyzed in **Fig. 4**, which was gradually increased by substituting the Ti with Nb as well. More specifically, the average diameter of precipitates in the Al_6Ti_4 HEA is 34.3 ± 7.5 nm, which is a little bit smaller than that in the Al_6Nb_4 HEA (37.0 ± 6.5 nm). Note that the $L1_2$ precipitates in the present alloy system could maintain a small particle size during the prolonged aging durations up to 336 h at 800 ℃. For instance, the Al_6Ti_4 HEA has a small size with an average diameter of 64.8 ± 17.2 nm. Moreover, for the shorter aging time (24 h) in **Fig. 3a**, the precipitates are near spheroidal. With the aging times going on, the precipitates keep the spheroidal morphology even after the long-term duration of 336 h (**Fig. 3d)**. With the substitution of Ti with Nb, the morphology of precipitates evolved from the spherical particles into the round-cornered cuboidal precipitates in the $Al_6Ti_2Nb_2$ HEA. As shown in **Figs. 3i-j**, a further increase of Nb substitution gradually promotes the cuboidal precipitate in the Al_6Nb_4 HEA. Collectively, both the size variation and the morphology transition of the $L1_2$ nanoparticles are affected by the chemical compositions.

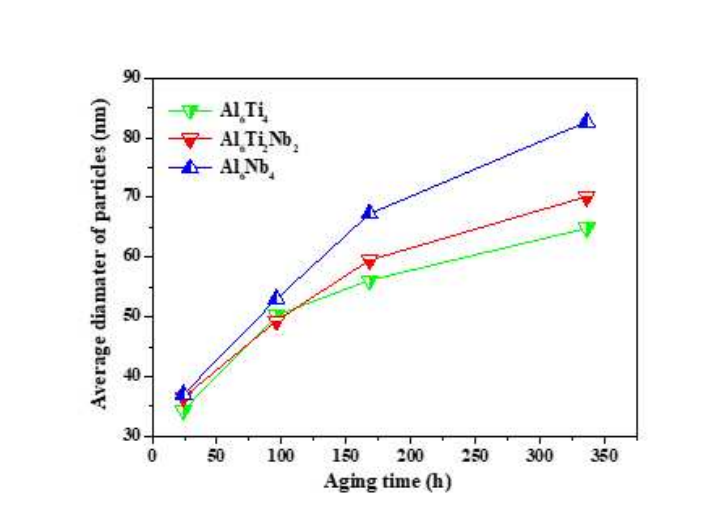

Fig. 4 The average diameters of the $L1_2$-type nanoparticles in the present HEAs after aging at 800 °C for various durations.

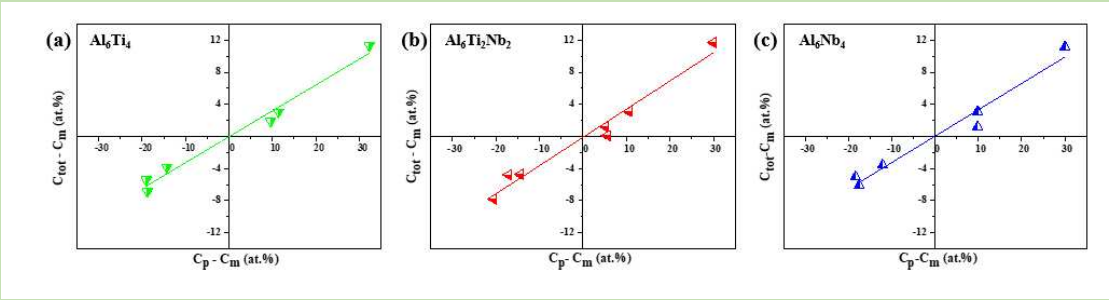

Fig. 5 Level rule for the calculation of the volume fraction of the intragranular nanoparticles in the (a) Al_6Ti_4, (b) $Al_6Ti_2Nb_2$, and (c) Al_6Nb_4 HEAs after aging at 800 ℃ for 24 h. (C_p: composition of the precipitate, C_m: composition of the matrix, C_{tot}: nominal total composition)

As given in **Fig. 5**, the volume fractions of the $L1_2$ phase for the specimens isothermally aged at 800 ℃ can be estimated to be around ~ 32.8%, 34.5%, and 32.8% by level rule in the Al_6Ti_4, $Al_6Ti_2Nb_2$, and Al_6Nb_4 HEAs, respectively. Note that the volume fractions of $L1_2$ nanoparticles in the Al_6Ti_4 and Al_6Nb_4 HEAs are relatively lower than that in the $Al_6Ti_2Nb_2$ HEA. The bulk composition of $Ni_{39.7}Co_{20.2}Cr_{15.2}Fe_{14.5}Al_{6.1}Ti_{2.1}Nb_{2.0}$ was derived by APT, which closely agrees with the nominal composition, making it accurate to obtain the volume fraction of ~ 34.5% of $L1_2$ phase by level rule in the $Al_6Ti_2Nb_2$ HEA. By contrast, the slightly decreased volume fractions in the Al_6Ti_4 and Al_6Nb_4 HEAs suggest that there are obvious elemental segregations or other type phases enriched with the $L1_2$-forming elements were formed at the grain boundary regions in those HEAs after the aging treatments.

3.3 Microstructural evolutions at the grain-boundary regions

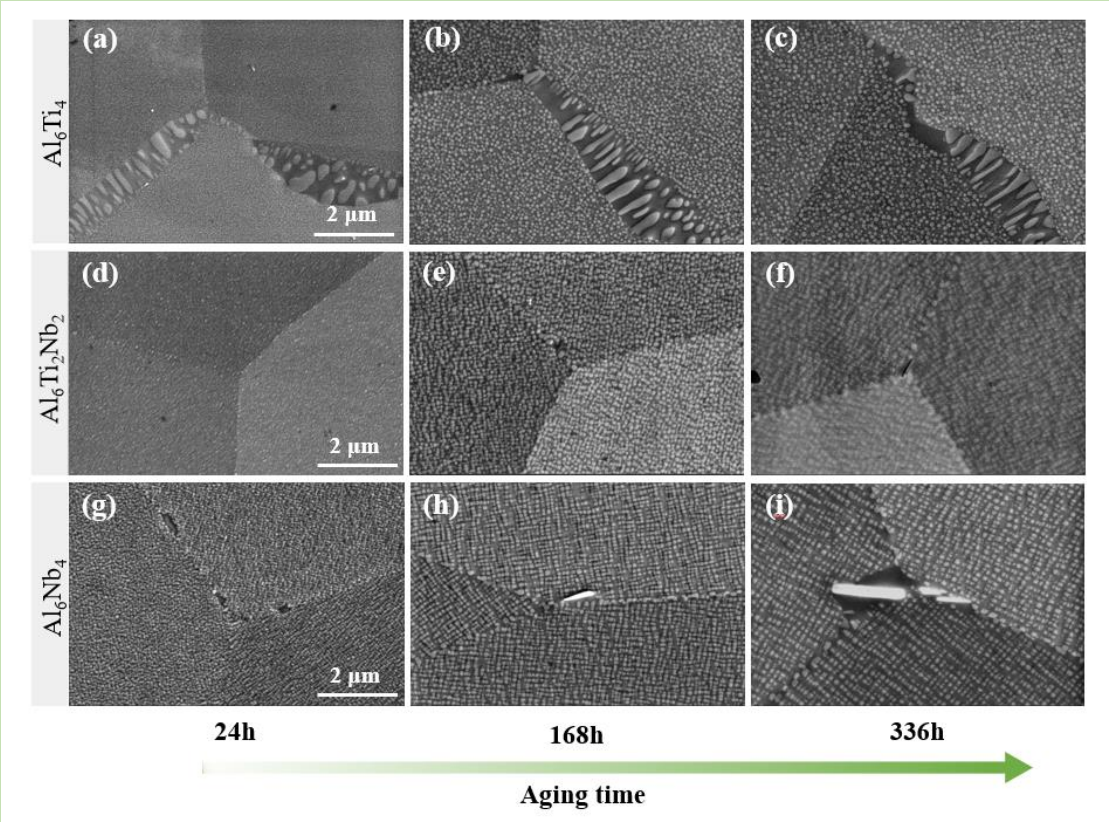

Fig. 6 The microstructural evolutions at the grain boundary triple junctions of the (a ~ c) Al_6Ti_4, (d ~ f) $Al_6Ti_2Nb_2$, and (g ~ i) Al_6Nb_4 HEAs upon aging at 800 °C for 24 h, 168 h, and 336 h.

Figure. 6 shows the representative SEM images of the HEAs at grain boundary regions after aging at 800 °C for various durations. The grain interiors of all three kinds of samples present the dual-phase "$L1_2$ + FCC" microstructure. However, a significant difference in the grain boundary morphologies can be clearly identified. After aging at 800 °C for 24 h, the Al_6Ti_4 HEA exhibits uniformly dispersed spherical nanoparticles in the grain interiors in **Fig. 6a**, whereas the grain boundary regions contain discontinuous cellular-shaped coarse colonies. With the promotion of aging time to 336 h, as given in **Fig. 6c,** the discontinuous and continuous regions still coexist in the Al_6Ti_4 HEA. This discontinuous precipitation observed in the grain boundary regions would cause the degradation of tensile strength at elevated temperatures, especially above 600 °C [20]. Interestingly, such a discontinuous precipitation behavior can be well eliminated by minor substitution of Ti by Nb, by which a pristine "$L1_2$ + FCC" dual-phase structure with no measurable precipitation of other intermetallic compound at the grain

boundaries was formed in the $Al_6Ti_2Nb_2$ HEA even after the long-term aging duration, as shown in **Figs. 6d-f**.

As shown in **Fig. 6g**, with the absolute substitution of Ti by Nb, a tiny amount of grain boundary-type phases were formed in the Al_6Nb_4 HEA after aging at 800 ℃ for 24 h due to the excessive addition of Nb [17]. However, after aging at 800 °C for 168 h, a new type of lamellae-structured phase (see **Fig. 6h**) with a length of about ~ 686 nm at grain boundaries was significantly promoted, which coarsens with the prolong of aging time to 336 h (see **Fig. 6i**).

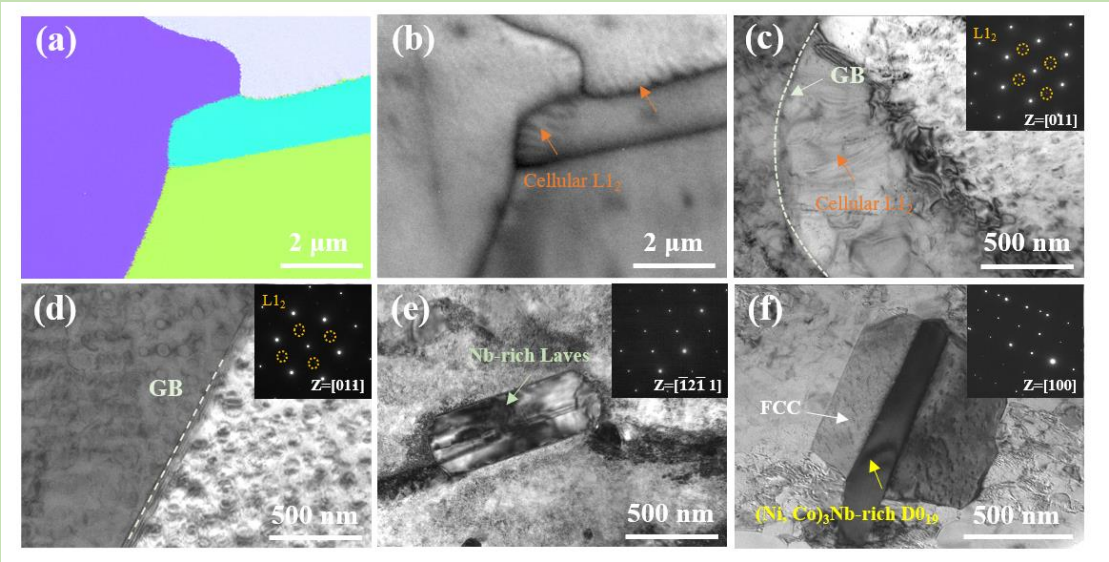

Fig. 7 The EBSD (a) inverse pole map and (b) band contrast map of the Al_6Ti_4 HEA at grain boundary region with discontinuous $L1_2$ precipitates after aging at 800 ℃ for 336 h. The TEM images showing the microstructural evolutions at the grain boundary triple junction: (c) Al_6Ti_4 HEA after aging at 800 ℃ for 336 h; (d) $Al_6Ti_2Nb_2$ HEA after aging at 800 ℃ for 336 h; (e) Al_6Nb_4 HEA after aging at 800 ℃ for 24 h; and (f) Al_6Nb_4 HEA after aging at 800 °C for 336 h. (GB: grain boundary)

In order to obtain further confirmation, TEM was employed to characterize the grain boundary-type precipitates in the present alloy system. The coherent relationship between the cellular particles and the FCC matrix in the Al_6Ti_4 HEA could be confirmed from the EBSD and TEM images in **Figs. 7a-c**. The formation of cellular precipitates results in the curvatures of grain boundaries in the Al_6Ti_4 HEA. By contrast, planar grain boundaries with no discontinuous

precipitation were observed by the TEM observation in the $Al_6Ti_2Nb_2$ HEA, as given in **Fig. 7d,** and no measurable other phases were found as well. The grain boundary-type phase in the Al_6Nb_4 HEA after aging at 800 °C for 24 h showed a hexagonal close-packed (HCP) diffraction, as shown in the insert in **Fig. 7e**, which can be indexed as the Laves phase with a composition of $Nb_{52.9}Cr_{21.8}Co_{9.4}Fe_{7.9}Ni_{7.1}Al_{0.8}$ (determined by the STEM-EDS analysis). Formation of this Laves phase consumes the $L1_2$-forming elements, including both Ni and Nb, thereby reducing the volume fraction accordingly in the Al_6Nb_4 HEA. The long-term aging-induced lamellae-type phase in the Al_6Nb_4 HEA was confirmed as the $D0_{19}$ phase from the diffraction patterns in **Fig. 7f**. Moreover, there are small FCC phases were found that sounded the lamellae phase, and the formation of lamellae phase always generates the small FCC-type grains with $L1_2$-free zones at the grain boundaries, which supports the observation that the lamellae-like precipitates appear to grow at the expense of strengthening $L1_2$ phase [21]. Likewise, the formation of lamellae-type $D0_{19}$ phase together with the $L1_2$-free zones leads to the serration of grain boundaries in the Al_6Nb_4 HEA, which is similar to that in the Allvac 718Plus [21].

3.4 Mechanical properties of the as-aged alloys at both room and elevated temperatures

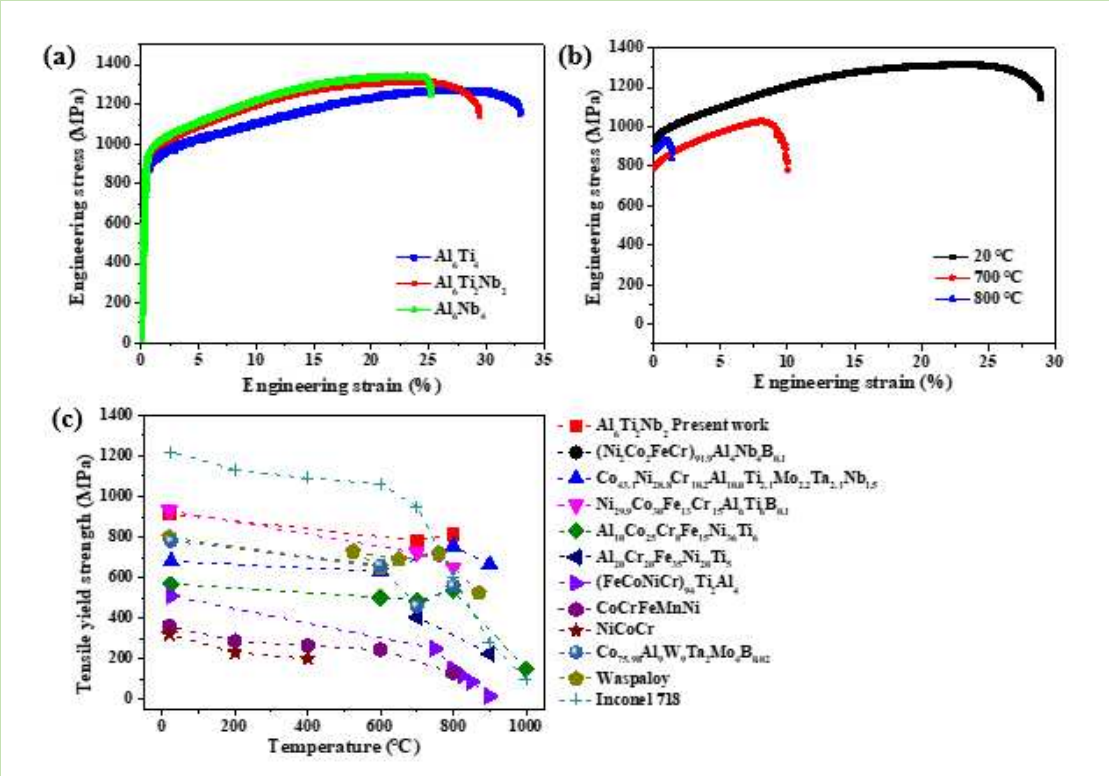

Fig. 8 Room-temperature tensile curves of the HEAs after aging at 800 °C for 24 h. (b) High-

temperature tensile curves for the $Al_6Ti_2Nb_2$ alloy. (c) Comparisons of yield strength as a function of test temperature.

Figure 8a displays the representative engineering stress-strain curves for the 24 h-aged HEAs tested at room temperature. The coherent precipitated $L1_2$ phases with high anti-phase boundary (APB) energy contribute to the high strength at room temperature [22]. As a result, the Al_6Ti_4 HEA has a yield strength of 857 ± 10 MPa and an ultimate strength of 1242 ± 5 MPa and high ductility of 30.3 ± 0.6%. Minor substitution of Ti by Nb could improve the yield strength and the ultimate strength to 915 ± 8 MPa and 1,291 ± 13 MPa in the Al_6Ti_2 Nb_2 HEA, respectively, along with a tensile ductility of 26.2 ± 1.2% at room temperature. By the further addition of Nb, an improved mechanical property (yield strength of 947 ± 8 MPa, ultimate strength of 1,339 ± 2 MPa) with a very small sacrifice of ductility was achieved in the Al_6Nb_4 HEA. Based on these results, it is concluded that the tensile strength of HEA could be slightly improved by the substitution of Ti with Nb.

In view of the stable phase component and the relatively better strength in the $Al_6Ti_2Nb_2$ HEA, the mechanical properties of the $Al_6Ti_2Nb_2$ alloy were studied at elevated temperatures. A high yield strength ($\sigma_{0.2}$) of 791 ± 7 MPa was achieved at 700 ℃ in **Fig. 8b**. What's more, this alloy processes an acceptable tensile ductility of 7.8 ± 0.5% at 700 ℃ along with high tensile strength of 1013 ± 11 MPa. However, a seriously decreased ductility was found when tested at 800 ℃. This kind of embrittlement behavior should be ascribed to the environmental damage by oxygen [23]. The stress-assisted diffusion of oxygen along grain boundaries decohesion the boundaries quickly due to the seriously decreased grain-boundary strength with the increase of temperatures [24]. Notably, of particular interest is that this alloy could stay at a high yield strength ($\sigma_{0.2}$) of 814 ± 39 MPa with an anomalous rise at 800 ℃. The occurrence of anomalous rise in the yield strength can also be found in several Ni and Co-based superalloys at elevated temperatures [25]. The high-temperature yield strengths of present HEAs and conventional metallic materials were given in **Fig. 8c**. In comparison with the single-phase CoCrFeMnNi and NiCoCr [26] HEAs, Co-based superalloys [27], Ni-based superalloys [19],

and other $L1_2$-type precipitation strengthened HEAs [28-31], the present $Al_6Ti_2Nb_2$ alloy possesses excellent yield strength at high-temperature ranges, clearly outperforming many advanced materials.

4. Discussion

4.1 Lattice misfit-induced differences on the morphology evolutions and coarsening kinetics of nanoprecipitates

As shown in **Fig. 3**, a minor substitution of Ti by Nb results in a spheroidal-to-cuboidal transition, indicating that the equilibrium morphology of coherent $L1_2$ precipitates depends on the chemical compositions. Typically, two competing factors, including the precipitate/matrix interfacial free energy and elastic strain energy, determine the equilibrium shape during the coarsening process in an alloy system [32]. The precipitate/matrix interfacial free energy contributes more to the morphology of nanoparticles at the very initial stage of aging due to the large specific surface area [33]. As can be seen from **Fig. 3**, all the particles have already evolved into the equilibrium morphologies after aging at 800 ℃ for 24 h, which suggests that the elastic strain energy takes the leading role in the determination of the equilibrium shape in this alloy system [34]. It is argued that the lattice misfit will influence the elastic strain energy between the FCC matrix and $L1_2$ particles, which in turn will affect the morphology and coarsening kinetics of the precipitates in these alloys [32]. **Fig. 9** shows the XRD patterns in the present alloy system, the enlarged sections in **Fig. 9** display the lattice misfit by deconvoluting the diffraction peak of (200) [35]. A relatively small lattice misfit of 0.15% was obtained in the Al_6Ti_4 HEA, and by substituting the Ti with Nb, a relatively larger lattice misfit of 0.54% was formed in the Al_6Nb_4 HEA. As argued that the larger value of the lattice misfit results in the larger elastic strain energy, thus the equilibrium morphology of the $L1_2$ phase can be changed accordingly [36].

A dimensionless parameter L was proposed by Thompson et al. to quantitatively describe the equilibrium morphology of a particle as [33]: $L = \varepsilon^2 C_{44} r/\sigma$, where ε is the lattice mismatch strain, which can be obtained from the XRD patterns. r is the average radius of the precipitates after aging at 800 ℃ for 24 h. σ is the interfacial energy between the FCC and $L1_2$

phases. C_{44} is an elastic constant of the matrix, which could be borrowed from Ni-based superalloys with a value of ~ 124 GPa [37]. As indicated in the Thompson's theory, the equilibrium shape of the spheroidal precipitate with a 4-fold symmetry is energy minima when $2 < L < 4$ [38]. Since the shape of the particle in the Al_6Ti_4 HEA maintains a spherical morphology, $L = 2$ can be used to estimate the lower bound of the interfacial energy of the Al_6Ti_4 HEA. Substituting the experimentally determined values, the interfacial energy was estimated to be around 5 mJ/m^2 for the Al_6Ti_4 HEA when aged at 800 °C. In contrast, the particles in the $Al_6Ti_2Nb_2$ and Al_6Nb_4 HEAs have round-cornered cuboidal precipitates with 4-fold symmetry. By using $L = 4$, the upper bound interfacial energy could be predicted to be 6.5 and 44 mJ/m^2 in the $Al_6Ti_2Nb_2$ and Al_6Nb_4 HEAs, respectively [16]. Thus, the interfacial energies of the present HEAs are relatively lower than that in the previous alloys [9]. So, in this study, Nb addition to the alloy increases the lattice misfit, by which the change in the morphology from spherical to round-cornered cuboidal shape occurred. This morphological change in shape is an outcome of the dominance of the elastic strain energy over the interfacial free energy in minimizing the total free energy in the present HEAs.

To quantitatively analyze the coarsening rate, a more generalized treatment of coarsening in multi-component alloys was proposed by Philippe and Voorhees (P-V) as [39]: $r^3 - r_0^3 = k(t - t_0)$, where k is the coarsening rate constant, r denotes the average radius of particles, t refers to the aging time. The P-V coarsening with a temporal exponent of 3 is more recognized for the coarsening of $L1_2$ particles [32]. For this reason, the relationship plot of radius vs. aging time for isothermal annealing at 800 ℃ was presented in **Fig. 10a**, from which relatively small coarsening rates of 2.47×10^{-29}m^3/s, 3.31×10^{-29}m^3/s, and 5.74×10^{-29}m^3/s were obtained in the Al_6Ti_4, $Al_6Ti_2Nb_2$, and Al_6Nb_4 HEAs, respectively. The coarsening rate of the $L1_2$ particles is dependent on the diffusion of the controlling solute and interfacial energy [40]. Evidently, from the diffusion point of view, the refractory Nb element with larger atomic size and higher melting point is the slowest diffusing solute when compared with the other solutes, which may help to slow down the coarsening rate [41].

In fact, the smaller lattice misfit in Al_6Ti_4 HEA contributes more to the microstructural stability by maintaining the smaller elastic stress during the coarsening process. With the

partition of Nb in the $L1_2$ phase, the larger lattice misfit exerts an higher interfacial energy [42]. Consequently, the substitution of Nb in the base alloy facilitates the coarsening of the $L1_2$ precipitates, demonstrating that lattice misfit dominates the differences in the coarsening rates in the present alloy system. Since the fast precipitation coarsening caused degradation of mechanical properties, microstructural stability with a slow coarsening rate is a necessity for high-temperature applications. A comparison between the present HEAs and traditional superalloys is plotted in **Fig. 10b**. Importantly, the coarsening rates of the $L1_2$ phase are lower than that of several HEAs and traditional Ni-based superalloys upon aging treatment at the same temperature of 800 °C. In present alloys, although the increased addition of Nb increases the coarsening rate, the high contents of rate-limiting elements of $L1_2$ phase (like Cr and Co) in the chemically complex HEAs can slow the coarsening rates [43]. As a result, the multi-component HEAs have a lower coarsening rate as compared to the chemically simpler traditional superalloys and other $L1_2$-strengthened HEAs [9, 44-48].

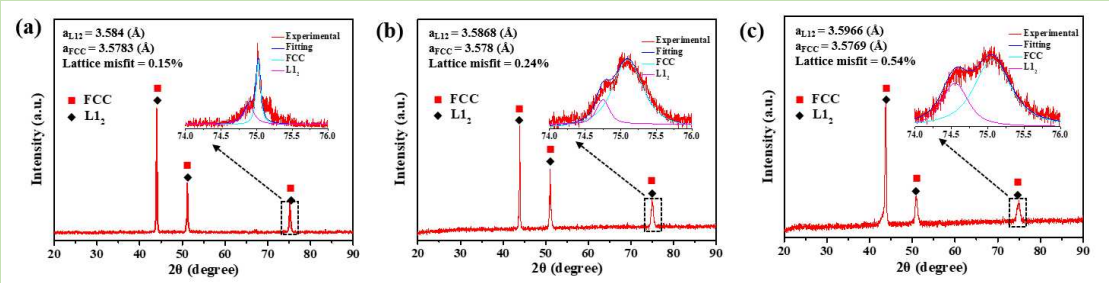

Fig. 9 XRD patterns of the (a) Al_6Ti_4, (b) $Al_6Ti_2Nb_2$, and (c) Al_6Nb_4 HEAs upon aging at 800 °C for 24 h. The inserts show the corresponding deconvolutions of the (220) diffraction peaks.

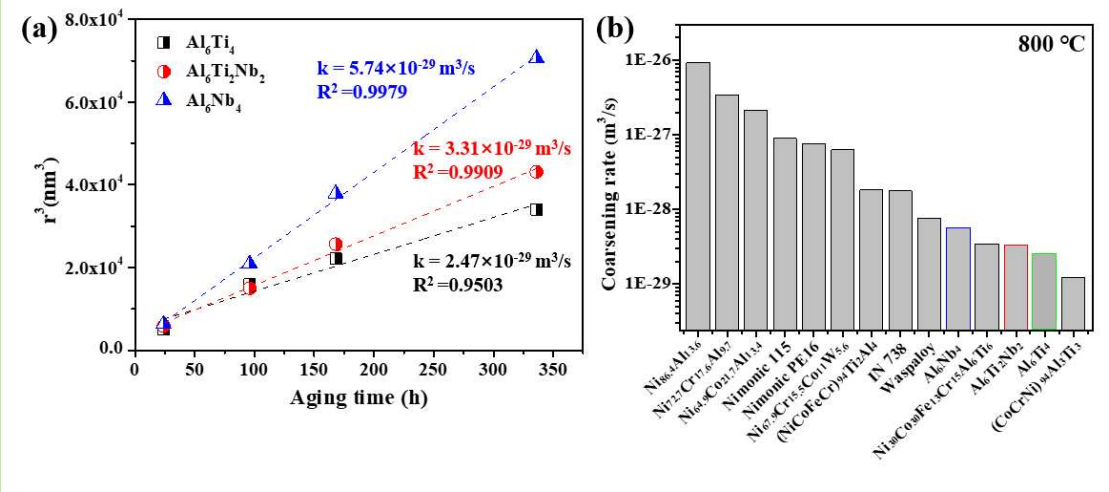

Fig. 10 (a) The P-V relationship illustrating the coarsening rates of the $L1_2$ nanoprecipitates. (b) Comparison of coarsening rates for the Ni-based superalloys and other HEAs at 800 °C [9, 44-48].

4.2 Locally compositional segregations-dominated microstructural evolutions in the grain boundary regions

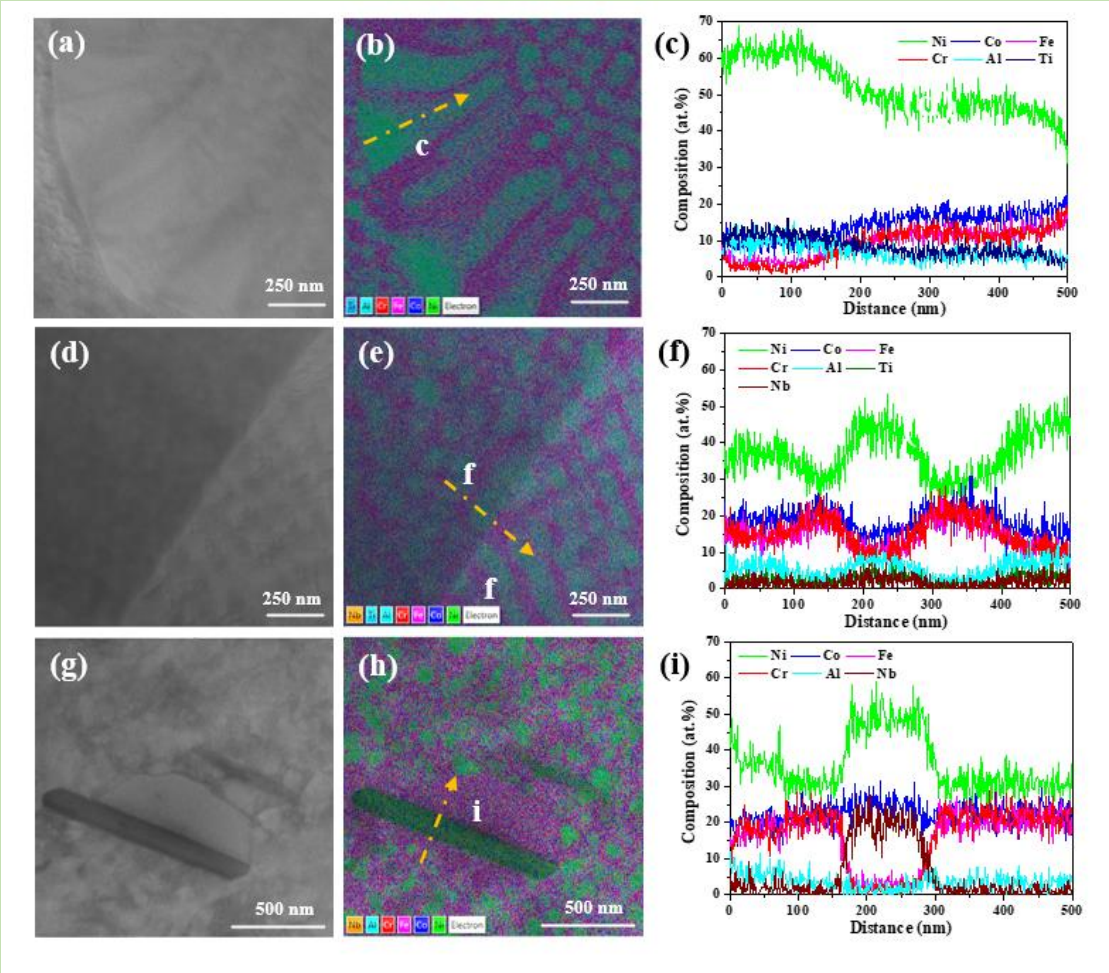

Fig. 11 The microstructural evolutions and corresponding elemental distributions at grain boundary regions after aging at 800 ℃ for 336 h. (a) STEM image and (b) all-elemental mixed map and (c) the corresponding line analysis across the cellular $L1_2$ phase in the grain-boundary region in the Al_6Ti_4 HEA. (d) STEM image and (e) all-elemental mixed map and the (d) corresponding line analysis across the cuboidal $L1_2$ phase at the grain boundary region in the $Al_6Ti_2Nb_2$ HEA. (g) STEM image and (h) all-elemental mixed map and the corresponding line analysis across the $D0_{19}$ phase in the grain-boundary region in the Al_6Nb_4 HEA.

The cellular-type precipitations have close correlations with the grain size, aging temperature and time, and chemical compositions in HEAs [17, 49]. In this part, the element-

mediated grain boundary precipitation behaviors are discussed. The discontinuous precipitation of $L1_2$ precipitates with a cellular shape grain boundary region was identified in the Al_6Ti_4 HEA, as shown in **Fig. 11a**. The formation of cellular $L1_2$ phase can be ascribed to a discontinuous-coarsening mechanism [50]. As confirmed by the STEM image in the **Fig. 11b,** the grain boundary segregation of Ni, Ti, and Al might be responsible for the occurrence of cellular reaction. The STEM lines analysis across the cellular $L1_2$ phase in **Fig. 11c** suggests that the discontinuous precipitation reaction requires the compositional supersaturation of $L1_2$-forming elements in the FCC matrix, especially the Ni, Ti, and Al [20]. The grain boundary segregation of Ni, Al, and Ti provides the chemical condition for the precipitation of $L1_2$ precipitates in the discontinuous mode. Note that the supersaturation of $L1_2$-forming elements at grain boundary regions always produces the Ni_2(Al, Ti)-type Heusler phase, which deteriorates the mechanical performances at elevated temperatures [9].

By contrast, the partial substitution of Ti by Nb greatly slows down the segregation tendency of Ti and Al elements at grain boundaries, driving the alloys with clean grain structure even after long-term aging duration. When compared with Ti, the element of Nb has been found that prefers to segregate at the grain-boundary region, by which the grain-boundary migration was suppressed greatly [17]. Due to the high melting point and large atomic diameter, the segregation of Nb could reduce the grain boundary energy and produce solute-drag effects, both of which substantially inhibit the discontinuous precipitates. Further increase in the substitution of Ti by Nb promotes the phase decomposition from the $L1_2$ to $D0_{19}$ phase at grain boundary regions upon the long-term aging process in the Al_6Nb_4 HEA. The much more addition of Nb inevitably generates the increased segregation of Nb at the grain boundary regions, which thereby promotes the formation of a Nb-rich $D0_{19}$ phase. Additionally, the coarsening of $L1_2$ phase requires the movement of Al and Nb, advancement of the grain boundary into the supersaturated grain collects Nb at the boundary, which is then consumed by the growing $D0_{19}$ lamellae. As given in our previous study, Al element is a vital ingredient to stabilize the $L1_2$ structure of the (Ni, Co, Fe, Cr)$_3$(Al, Nb)-type phase, the diffusion of Al in the matrix phase leaves the Nb-enriched region, thereby promoting the formation of the $D0_{19}$ phase as well [29]. The chemical composition distribution maps using STEM-EDS are given in **Fig. 11h.** The

surrounding regions with an FCC structure are given in **Fig. 11i,** where Ni, Co, Fe, and Cr were found to become rich in this region. The observation supports the fact that the lamellae-like $D0_{19}$ phase appears to grow at the expense of the $L1_2$ phase.

Generally, the transformation in ordered intermetallic crystal structure displays strong correlations with the valence electron concentration (VEC) of the phase. In detail, the lattice transforms from tetragonal to hexagonal and then to cubic structures with the decrease of VEC [51]. Specifically, as given in **Fig. 12a**, the tetragonal structure ($D0_a$ and $D0_{22}$) prefers to form at higher VEC (> 8.75), the pure hexagonal structure forms when VEC is close to 8.5, and the $L1_2$ structure tends to emerge at lower VEC (< 8.25). By implying the detailed chemical compositions in this study, we found that the VEC values of $Al_6Nb_2Ti_4$ and Al_6Nb_4 alloys are relatively lower, which presents a minor increase in the Al_6Ti_4 alloy. Thus, the minor addition of Nb is favored to stable the $L1_2$ structure. Strikingly, the VEC of the $D0_{19}$ phase in the Al_6Nb_4 alloy is quite close to the critical value of 8.54, which is consistent with the VEC value of hexagonal structure.

The phase stability of the alloy system with different Ti/Nb ratios at 800 °C was also evaluated by the CALPHAD (CALculation of PHAse Diagrams) method in **Fig. 12b** [52]. The corresponding isothermal phase diagram of the alloy system at 800 °C shows that as the concentration of Nb further increases to about ~ 3.4, the excessive Nb addition would promote the formation of the δ phase at the expense of the $L1_2$ particle. The phase transformations of $L1_2 \rightarrow \delta$ are commonly found in Ni-based superalloys, resulting in quick softening above 650 °C [53]. Being different from the predicted phase structure, a lamellae-structured phase with a stoichiometry of $Ni_{48.3}Co_{25.5}Fe_{2.9}Cr_{2.4}Al_{1.6}Nb_{19.9}$ as the $D0_{19}$ phase was initially formed when the alloy was aged at 800 ℃ for the long-term duration. From the CALPHAD analysis, the δ phase having superior thermodynamic stability upon long-term aging was predicted as the equilibrium phase when compared with the $D0_{19}$ in the Al_6Nb_4 HEA. Additionally, the metastable $D0_{19}$ phase would be transferred into the δ phase in the $Co_{1.5}FeNi_2V_{0.18}Nb_{0.19}Ta_{0.2}$ HEA upon aging at 900 ℃ for 3 days [54]. Based on the above analysis, the element-mediated microstructural evolutions upon long-term durations at grain boundary regions can be schematically illustrated in **Fig. 12c**.

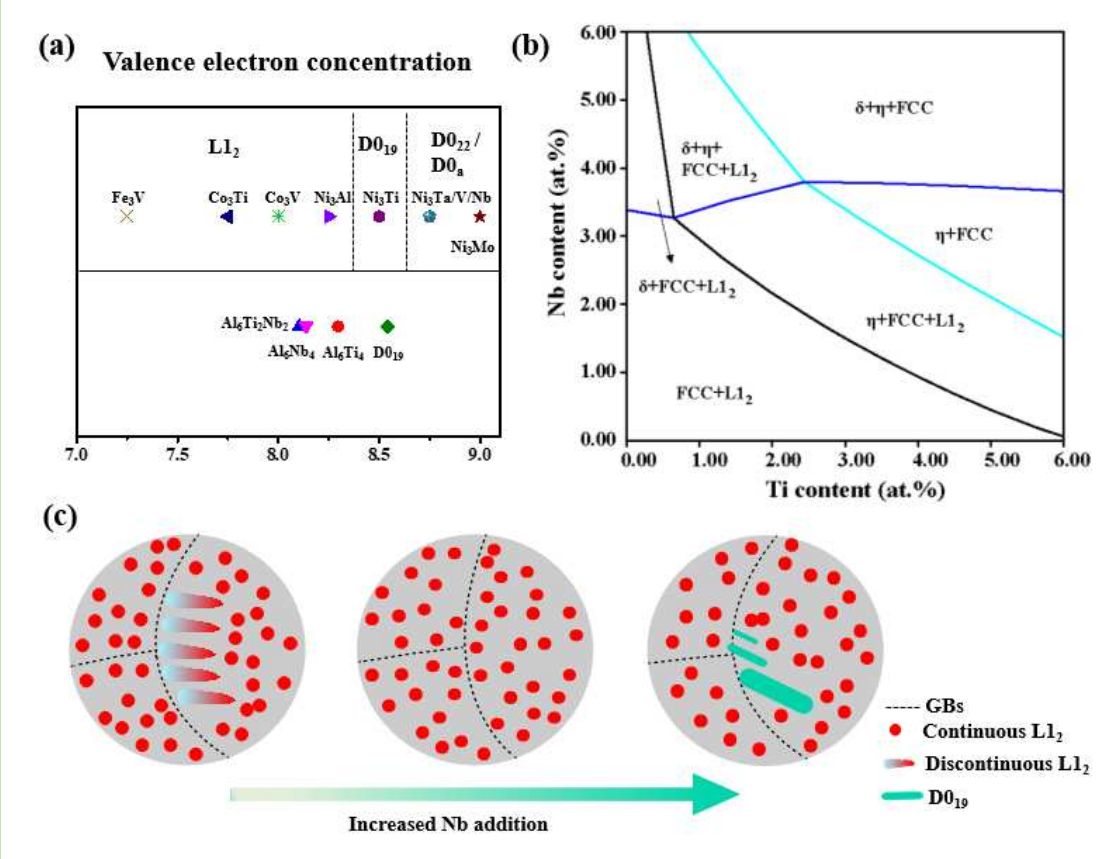

Fig. 12 (a) Valence electron concentrations in various ordered intermetallic phases. (b) Thermodynamic calculations showing the effects of Ti and Nb additions on the phase stabilities in the present system aged at 800 °C. (c) Schematic illustration showing the precipitation characteristics at the grain boundaries (GBs) after long-term aging at 800 ℃ in the present alloy system.

4.3 The deformation mechanisms at room and elevated temperatures

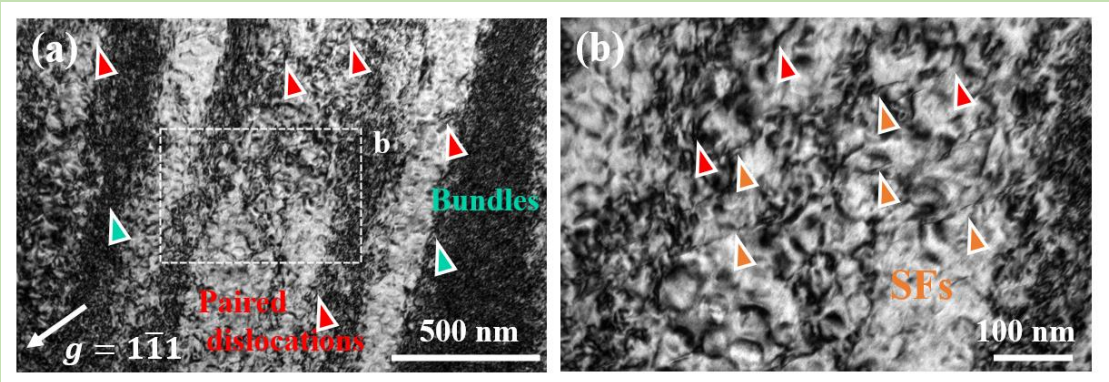

Fig. 13 (a) and (b) Bright-field TEM images of the post-tensile $Al_6Ti_2Nb_2$ HEA at room temperature captured under two-beam conditions, which are close to [110] zone axis. (SFs: Stacking faults)

For a better understanding of mechanical responses in the $Al_6Ti_2Nb_2$ HEA, the TEM was conducted to in-depth analyze the deformation mechanisms at both room and elevated temperatures. As given in **Fig. 13a**, planar dislocations gliding on the (111) planes are prevalent in the post-tensile $Al_6Ti_2Nb_2$ HEA, with the dislocation bundles being formed. The paired dislocation appears to accumulate at the dislocation bundles due to the strong coupling with the nanoparticles in the alloy with medium stacking fault energy (SFE) in the matrix phase [55]. The SFE of the matrix phase in the $Al_6Ti_2Nb_2$ HEA could be empirically estimated to be 38.3 mJ/m^2, which may play a key role in dominating the deformation mechanisms [56]. Paired dislocations are preferred to form in the $L1_2$-strengthened HEA with high SFE, whilst the stacking faults (SFs) are favored in the alloy with low SFE in the matrix phase [57]. Moreover, the planar SFs were observed in the $Al_6Ti_2Nb_2$ HEA, as shown in **Fig. 13b.** Collectively, both the pair of dislocations and the stacking faults are found to contribute to the deformations at room temperature.

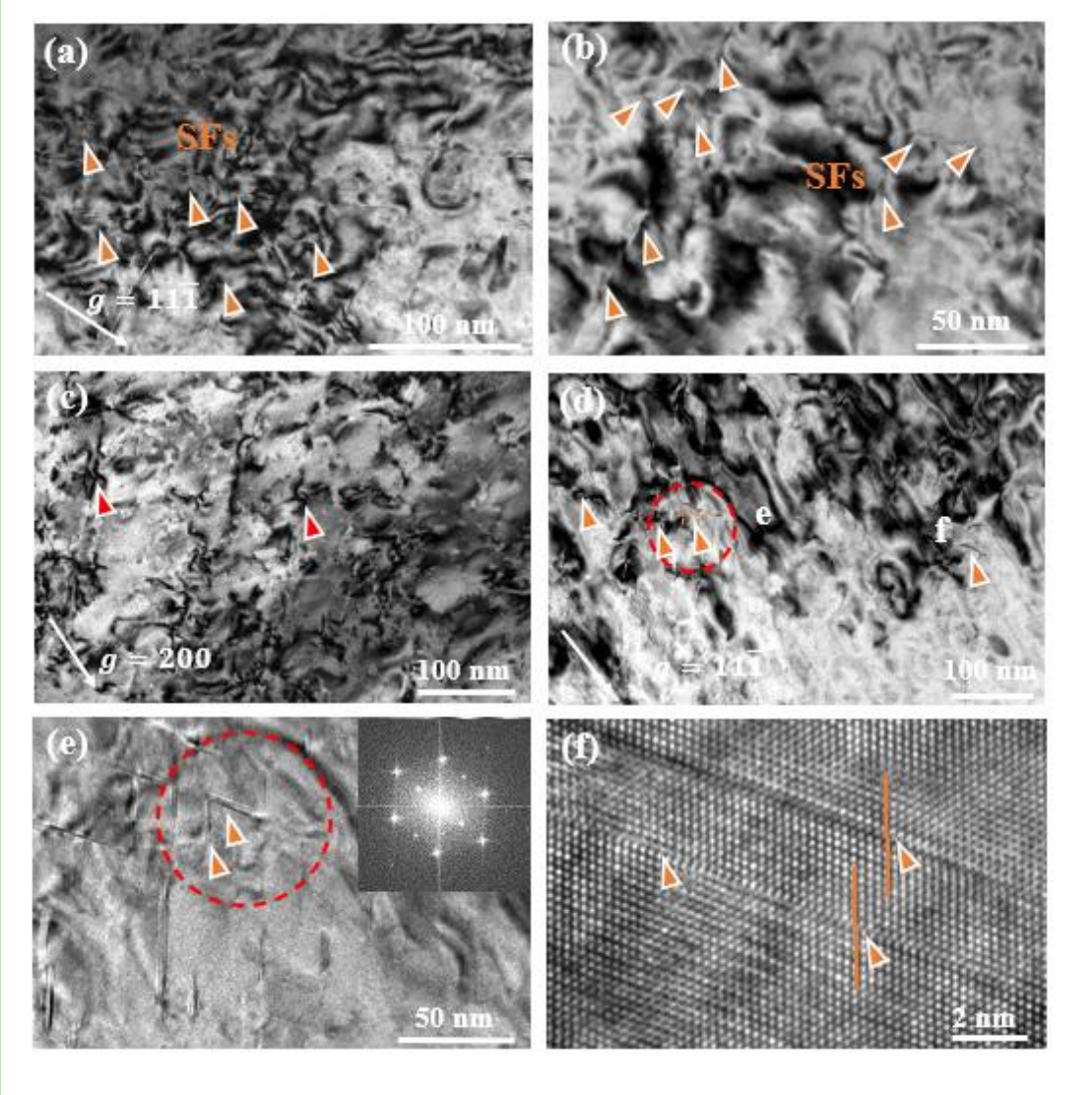

Fig. 14 (a) and (b) Bright-filed TEM images revealing the SFs-prevailed deformation process at 700 ℃. (c) and (d) Bright-filed TEM images of the deformed alloys at 800 ℃. (e) Magnified and (f) high-resolution TEM (HRTEM) images in (d) demonstrating the extension of the stacking faults within $L1_2$ particles via partial dislocations at 800 ℃. (SFs: Stacking faults)

As presented in **Fig. 14a**, planar-structured stacking faults were more likely to be activated at 700 ℃, which originated from the matrix and then span across the precipitates, leaving behind the superlattice stacking faults (SSFs) within the nanoparticles. These SFs were characterized by the configuration of planar glide along two non-coplanar slip systems, forming nano-spaced SFs nets in the enlarged view in **Fig. 14b**. The formation of SFs nets can dynamically refine the original grain, which contributes to a high strain-hardening rate during

the deformation [57]. This mechanism is consistent with the conventional superalloys in which shearing of precipitates by pair of a/2⟨110⟩ dislocations occurred at the low temperature, while the SFs formation by the movement of a/3⟨211⟩ partial dislocations prevailed at intermediate temperature range (about 600 °C ~ 800 °C) [58, 59].

At 800 °C, in addition to the paired dislocations in **Fig. 14c**, the slipping of SFs on the (111) plane is still believed as the main deformation mode, as indicated in **Fig. 14d**. Note that the multi-layered SFs were found in the particles, confirming the activation of multiple slip systems in the particles in **Fig. 14d**. More remarkably, SSFs with cross-slip configurations were nucleated in the $L1_2$ particles, as highlighted in **Fig. 14e**, which prevented the further expansion of the SSFs. **Fig. 14f** gives the HRTEM image in **Fig. 14d**, which clearly demonstrates the formations of the SFs within the particles. These strengthening mechanisms are similar to the thermally-assisted cross-slip of the screw segments at a peak temperature of yield anomaly in traditional Ni-based alloys [60]. Thus, the anomalous growth in yield strength can be ascribed to the activation of multi-layered SFs with cross-slip configuration in the particles at 800 °C.

5. Conclusion

In this study, the precipitate morphology, coarsening kinetics, grain structure, mechanical properties, and deformation mechanisms are explored in a series of $L1_2$-strengthened HEAs with multi-component $(Ni, Co, Fe, Cr)_3(Al, Ti, Nb)$-type $L1_2$ phase. We find that:

1. Nb addition in the present alloy system led to an obvious increase of the lattice misfit by around ~ 3.6 times that resulted in a change in the morphology of the $L1_2$ phase from spheroidal to round-cornered cuboidal precipitates along with an increase in the coarsening rate from $2.47 \times 10^{-29} m^3/s$ to $5.74 \times 10^{-29} m^3/s$ at 800 °C.
2. A discontinuous $L1_2$ phase with cellular morphology was formed in the $Ni_3(Al, Ti)$-type $L1_2$-strengthened HEA due to the elemental segregation at grain boundaries, which could be successfully eliminated by minor substitution of Ti by Nb, leaving a clean grain-boundary structure in the $Al_6Nb_2Ti_2$ HEA even upon long-term aging at 800 °C.
3. The excessive addition of Nb introduced the undissolved Nb-rich Laves phase in the Al_6Nb_4 HEA, upon long-term aging, which promotes the phase transformation from

$L1_2$ to the $D0_{19}$ phase.

4. The dislocation bundles, paired dislocations, and stacking faults dominate the deformation mechanism in the $Al_6Nb_2Ti_2$ HEA with medium SFE in the matrix phase at room temperature.
5. The coherent precipitation-strengthened $Al_6Nb_2Ti_2$ HEA displays a high yield strength of 797 MPa at 700 ℃, and the SFs-mediated deformation enables a superior high work-hardening rate, finally achieving a high ultimate strength of 1020 MPa. The nucleate of multi-layered SSFs within the particles contributes to the anomalous improvement in the yield strength at 800 ℃.

6. Acknowledgements

This work was financially supported by the National Natural Science Foundation of China (Grant no: 52101135), and the Hong Kong Research Grant Council, University Grants Committee (RGC) with CityU grants 21205621. We also thank the financial support from the CityU Shenzhen Research Institute (SRI) (Grant no: 2020A1515110647). PKL very much appreciates the support from (1) the National Science Foundation (DMR – 1611180, 1809640, and 2226508) and (2) the US Army Research Office (W911NF-13–1-0438 and W911NF-19–2-0049).

7. References

[1] J.X. Hou, B.X. Cao, B. Xiao., Z.B. Jiao, T. Yang. Compositionally complex coherent precipitation-strengthened high-entropy alloys: A critical review, Rare Metals (2022).

[2] B.H. Kear, E.R. Thompson. Aircraft Gas Turbine Materials and Processes, Science 208 (1980) 847-856.

[3] B. Geddes, H. Leon, X. Huang. Superalloys: Alloying and Performance. ASM International, 2010.

[4] T. Yang, Y.L. Zhao, Y. Tong, Z.B. Jiao, J. Wei, J.X. Cai, X.D. Han, D. Chen, A. Hu, J.J. Kai, K. Lu, Y. Liu, C.T. Liu. Multicomponent intermetallic nanoparticles and superb mechanical behaviors of complex alloys, Science 362 (2018) 933-937.

[5] J. Joseph, M. Annasamy, S.R. Kada, P.D. Hodgson, M.R. Barnett, D.M. Fabijanic. Optimising the Al and Ti compositional window for the design of γ' (L12)-strengthened Al–Co–Cr–Fe–Ni–Ti high entropy alloys, Materials Science and Engineering: A 835 (2022) 142620.

[6] J. Wang, J. Zou, H. Yang, X. Dong, P. Cao, X. Liao, Z. Liu, S. Ji. Ultrastrong and ductile (CoCrNi)94Ti3Al3 medium-entropy alloys via introducing multi-scale heterogeneous structures, Journal of Materials Science & Technology 135 (2023) 241-249.

[7] B. Xiao, J. Luan, S. Zhao, L. Zhang, S. Chen, Y. Zhao, L. Xu, C.T. Liu, J.-J. Kai, T. Yang. Achieving thermally stable nanoparticles in chemically complex alloys via controllable sluggish lattice diffusion, Nature Communications 13 (2022) 4870.
[8] T. Yang, Y.L. Zhao, W.H. Liu, J.H. Zhu, J.J. Kai, C.T. Liu. Ductilizing brittle high-entropy alloys via tailoring valence electron concentrations of precipitates by controlled elemental partitioning, Materials Research Letters 6 (2018) 600-606.
[9] T. Yang, Y.L. Zhao, L. Fan, J. Wei, J.H. Luan, W.H. Liu, C. Wang, Z.B. Jiao, J.J. Kai, C.T. Liu. Control of nanoscale precipitation and elimination of intermediate-temperature embrittlement in multicomponent high-entropy alloys, Acta Materialia 189 (2020) 47-59.
[10] K. Zhang, F. He, Z. Yang, D. Cui, J. Li, Z. Yang, J. Wang, Z. Wang. Effect of Re and Ru on the phase stability and coarsening kinetics of L12 phase in a Ni29Co27Fe27Cr3Al7Ti7 high entropy alloy, Journal of Alloys and Compounds 866 (2021) 158904.
[11] A.C. Yeh, T.K. Tsao, Y.J. Chang, K.C. Chang, J.W. Yeh, M.S. Chiou, S.R. Jian, C.M. Kuo, W.R. Wang, H. Murakami. Developing New Type of High Temperature Alloys–High Entropy Superalloys, Journal of Metallurgical and Materials Engineering 1 (2015).
[12] J. Zhang, T. Huang, K. Cao, J. Chen, H. Zong, D. Wang, J. Zhang, J. Zhang, L. Liu. A correlative multidimensional study of γ′ precipitates with Ta addition in Re-containing Ni-based single crystal superalloys, Journal of Materials Science & Technology 75 (2021) 68-77.
[13] X. Wu, S.K. Makineni, C.H. Liebscher, G. Dehm, J. Rezaei Mianroodi, P. Shanthraj, B. Svendsen, D. Burger, G. Eggeler, D. Raabe, B. Gault. Unveiling the Re effect in Ni-based single crystal superalloys, Nat Commun 11 (2020) 389.
[14] F. He, D. Chen, B. Han, Q. Wu, Z. Wang, S. Wei, D. Wei, J. Wang, C.T. Liu, J.-j. Kai. Design of D022 superlattice with superior strengthening effect in high entropy alloys, Acta Materialia 167 (2019) 275-286.
[15] Z. Liang, S. Neumeier, Z. Rao, M. Göken, F. Pyczak. CALPHAD informed design of multicomponent CoNiCr-based superalloys exhibiting large lattice misfit and high yield stress, Materials Science and Engineering: A 854 (2022) 143798.
[16] H. Zhang, C. Li, Y. Liu, Q. Guo, Y. Huang, H. Li, J. Yu. Effect of hot deformation on γ″ and δ phase precipitation of Inconel 718 alloy during deformation&isothermal treatment, Journal of Alloys and Compounds 716 (2017) 65-72.
[17] L. Fan, T. Yang, J.H. Luan, Z.B. Jiao. Control of discontinuous and continuous precipitation of γ′-strengthened high-entropy alloys through nanoscale Nb segregation and partitioning, Journal of Alloys and Compounds 832 (2020) 154903.
[18] P. Pandey, A.K. Sawant, B. Nithin, Z. Peng, S.K. Makineni, B. Gault, K. Chattopadhyay. On the effect of Re addition on microstructural evolution of a CoNi-based superalloy, Acta Materialia 168 (2019) 37-51.
[19] J.R. Davis. Nickel, Cobalt, and Their Alloys., ASM Specialty Handbook (2000) 44073. -44070 44070 44002 .
[20] C.-M. Kuo, C.-W. Tsai. Effect of cellular structure on the mechanical property of Al0.2Co1.5CrFeNi1.5Ti0.3 high-entropy alloy, Mater. Chem. Phys. 210 (2018) 103-110.
[21] E.J. Pickering, H. Mathur, A. Bhowmik, O.M.D.M. Messé, J.S. Barnard, M.C. Hardy, R. Krakow, K. Loehnert, H.J. Stone, C.M.F. Rae. Grain-boundary precipitation in Allvac 718Plus, Acta Materialia 60 (2012) 2757-2769.
[22] O. Gorbatov, I. Lomaev, Y. Gornostyrev, A. Ruban, D. Furrer, V. Venkatesh, D. Novikov, S.

Burlatsky. Effect of composition on antiphase boundary energy in Ni3Al based alloys: Ab initio calculations, Physical Review B 93 (2016) 224106.
[23] U. Krupp. Dynamic Embrittlement — Time–dependent Quasi–brittle Intergranular Fracture at High Temperatures, International Materials Reviews 50 (2005) 83-97.
[24] K.S. Chan. A Grain Boundary Fracture Model for Predicting Dynamic Embrittlement and Oxidation-Induced Cracking in Superalloys, Metallurgical and Materials Transactions A 46 (2015) 2491-2505.
[25] T. Yang, B.X. Cao, T.L. Zhang, Y.L. Zhao, W.H. Liu, H.J. Kong, J.H. Luan, J.J. Kai, W. Kuo, C.T. Liu. Chemically complex intermetallic alloys: A new frontier for innovative structural materials, Materials Today (2021).
[26] Z. Wu, H. Bei, G.M. Pharr, E.P. George. Temperature dependence of the mechanical properties of equiatomic solid solution alloys with face-centered cubic crystal structures, Acta Materialia 81 (2014) 428-441.
[27] F. Zhong, S. Li, J. Sha. Tensile behaviour of Co–Al–W–Ta–B–Mo alloys with a coherent γ/γ' microstructure at room and high temperatures, Materials Science and Engineering: A 637 (2015) 175-182.
[28] B.X. Cao, H.J. Kong, Z.Y. Ding, S.W. Wu, J.H. Luan, Z.B. Jiao, J. Lu, C.T. Liu, T. Yang. A novel L12-strengthened multicomponent Co-rich high-entropy alloy with both high γ′-solvus temperature and superior high-temperature strength, Scripta Materialia 199 (2021) 113826.
[29] Y.L. Zhao, T. Yang, Y.R. Li, L. Fan, B. Han, Z.B. Jiao, D. Chen, C.T. Liu, J.J. Kai. Superior high-temperature properties and deformation-induced planar faults in a novel L12-strengthened high-entropy alloy, Acta Materialia 188 (2020) 517-527.
[30] J.Y. He, H. Wang, Y. Wu, X.J. Liu, T.G. Nieh, Z.P. Lu. High-temperature plastic flow of a precipitation-hardened FeCoNiCr high entropy alloy, Materials Science and Engineering: A 686 (2017) 34-40.
[31] H.M. Daoud, A.M. Manzoni, N. Wanderka, U. Glatzel. High-Temperature Tensile Strength of Al10Co25Cr8Fe15Ni36Ti6 Compositionally Complex Alloy (High-Entropy Alloy), Jom 67 (2015) 2271-2277.
[32] S. Meher, S. Nag, J. Tiley, A. Goel, R. Banerjee. Coarsening kinetics of γ′ precipitates in cobalt-base alloys, Acta Materialia 61 (2013) 4266-4276.
[33] M.E. Thompson, C.S. Su, P.W. Voorhees. The equilibrium shape of a misfitting precipitate, Acta Metallurgica et Materialia 42 (1994) 2107-2122.
[34] W.C. Johnson, J.W. Cahn. Elastically induced shape bifurcations of inclusions, Acta Metallurgica 32 (1984) 1925-1933.
[35] D.M. Collins, L. Yan, E.A. Marquis, L.D. Connor, J.J. Ciardiello, A.D. Evans, H.J. Stone. Lattice misfit during ageing of a polycrystalline nickel-base superalloy, Acta Materialia 61 (2013) 7791-7804.
[36] R.C. Ecob, R.A. Ricks, A.J. Porter. The measurement of precipitate/matrix lattice mismatch in nickel-base superalloys, Scripta Metallurgica 16 (1982) 1085-1090.
[37] H. Pottebohm, G. Neite, E. Nembach. Elastic properties (the stiffness constants, the shear modulus and the dislocation line energy and tension) of Ni□Al solid solutions and of the Nimonic alloy PE16, Materials Science and Engineering 60 (1983) 189-194.
[38] C.K. Sudbrack, T.D. Ziebell, R.D. Noebe, D.N. Seidman. Effects of a tungsten addition on the morphological evolution, spatial correlations and temporal evolution of a model Ni–Al–Cr superalloy, Acta Materialia 56 (2008) 448-463.

[39] T. Philippe, P.W. Voorhees. Ostwald ripening in multicomponent alloys, Acta Materialia 61 (2013) 4237-4244.
[40] K. Kim, P.W. Voorhees. Ostwald ripening of spheroidal particles in multicomponent alloys, Acta Materialia 152 (2018) 327-337.
[41] D.B. Miracle, O.N. Senkov. A critical review of high entropy alloys and related concepts, Acta Materialia 122 (2017) 448-511.
[42] F. He, K. Zhang, G. Yeli, Y. Tong, D. Wei, J. Li, Z. Wang, J. Wang, J.-j. Kai. Anomalous effect of lattice misfit on the coarsening behavior of multicomponent L12 phase, Scripta Materialia 183 (2020) 111-116.
[43] X. Zhuang, S. Antonov, L. Li, Q. Feng. Effect of alloying elements on the coarsening rate of γ′ precipitates in multi-component CoNi-based superalloys with high Cr content, Scripta Materialia 202 (2021) 114004.
[44] Y.Y. Zhao, H.W. Chen, Z.P. Lu, T.G. Nieh. Thermal stability and coarsening of coherent particles in a precipitation-hardened (NiCoFeCr)94Ti2Al4 high-entropy alloy, Acta Materialia 147 (2018) 184-194.
[45] X. Li, N. Saunders, A.P. Miodownik. The coarsening kinetics of γ′ particles in nickel-based alloys, Metallurgical and Materials Transactions A 33 (2002) 3367-3373.
[46] J.S. Hou, J.T. Guo, G.X. Yang, L.Z. Zhou, X.Z. Qin, H.Q. Ye. The microstructural instability of a hot corrosion resistant superalloy during long-term exposure, Materials Science and Engineering: A 498 (2008) 349-358.
[47] Y. Zhao, T. Yang, B. Han, J. Luan, D. Chen, W. Kai, C.T. Liu, J.-j. Kai. Exceptional nanostructure stability and its origins in the CoCrNi-based precipitation-strengthened medium-entropy alloy, Materials Research Letters 7 (2019) 152-158.
[48] H. Bian, X. Xu, Y. Li, Y. Koizumi, Z. Wang, M. Chen, K. Yamanaka, A. Chiba. Regulating the coarsening of the γ′ phase in superalloys, NPG Asia Materials 7 (2015) e212-e212.
[49] J.Y.C. Fang, W.H. Liu, J.H. Luan, T. Yang, Y. Wu, M.W. Fu, Z.B. Jiao. Competition between continuous and discontinuous precipitation in L12-strengthened high-entropy alloys, Intermetallics 149 (2022) 107655.
[50] H. Ramanarayan, T.A. Abinandanan. Grain boundary effects on spinodal decomposition: II. Discontinuous microstructures, Acta Materialia 52 (2004) 921-930.
[51] C.T. Liu, J.O. Stiegler. Ductile Ordered Intermetallic Alloys, Science 226 (1984) 636-642.
[52] J.O. Andersson, T. Helander, L. Höglund, P. Shi, B. Sundman. Thermo-Calc & DICTRA, computational tools for materials science, Calphad 26 (2002) 273-312.
[53] O.M. Messé, J.S. Barnard, E.J. Pickering, P.A. Midgley, C.M.F. Rae. On the precipitation of delta phase in ALLVAC® 718Plus, Philosophical Magazine 94 (2014) 1132-1152.
[54] G.H. Xia, Z.L. Ma, Z.Q. Xu, M. Wang, X.W. Cheng, H.N. Cai. Novel high-entropy alloys with high-density ε-D019 and abnormal phase transformation, Scripta Materialia 199 (2021) 113893.
[55] D. Raynor, J.M. Silcock. Strengthening Mechanisms in γ′ Precipitating Alloys, Metal Science Journal 4 (1970) 121-130.
[56] X.S. Xie, G.L. Chen, P.J. McHugh, J.K. Tien. Including stacking fault energy into the resisting stress model for creep of particle strengthened alloys, Scripta Metallurgica 16 (1982) 483-488.
[57] J.X. Hou, S.F. Liu, B.X. Cao, J.H. Luan, Y.L. Zhao, Z. Chen, Q. Zhang, X.J. Liu, C.T. Liu, J.J. Kai, T. Yang. Designing nanoparticles-strengthened high-entropy alloys with simultaneously enhanced strength-ductility synergy at both room and elevated temperatures, Acta Materialia (2022) 118216.

[58] T. Peng, Y. Wang, B. Yang, G. Yang. Tensile properties and deformation mechanisms of nimonic 105 superalloy at different temperatures, Materials Science and Engineering: A 828 (2021) 142028.
[59] D. Barba, E. Alabort, S. Pedrazzini, D.M. Collins, A.J. Wilkinson, P.A.J. Bagot, M.P. Moody, C. Atkinson, A. Jérusalem, R.C. Reed. On the microtwinning mechanism in a single crystal superalloy, Acta Materialia 135 (2017) 314-329.
[60] W. Li, J. Ma, H. Kou, J. Shao, X. Zhang, Y. Deng, Y. Tao, D. Fang. Modeling the effect of temperature on the yield strength of precipitation strengthening Ni-base superalloys, International Journal of Plasticity 116 (2019) 143-158.